Observations of Large Wind Shear above the Marine Boundary Layer near Point Buchon, California

DAVID A. RAHN

Department of Geography and Atmospheric Science, University of Kansas, Lawrence, Kansas

THOMAS R. PARISH AND DAVID LEON

Department of Atmospheric Science, University of Wyoming, Laramie, Wyoming

(Manuscript received 7 December 2015, in final form 7 April 2016)

ABSTRACT

Particularly strong winds along the coast of Southern California on 24 May 2012 were measured by the Wyoming King Air research aircraft during the Precision Atmospheric Marine Boundary Layer Experiment (PreAMBLE). The fast flow is bounded laterally by the coastal topography and vertically by a pronounced temperature inversion separating the cool, moist air in the marine boundary layer (MBL) from the warm, dry air aloft. Many studies have investigated the response of this two-layer flow to changes in the coastline by invoking hydraulic theory, which explains the essential characteristics including changes in MBL depth and the attendant wind. Processes occurring just above the MBL are important to the low-level thermodynamic and kinematic structure. Observations on this day demonstrate how the large shear above the MBL can impact the lower atmosphere. A typical two-layer system was observed north of Point Buchon, which was supercritical. Around Point Buchon, the depth of the MBL decreased and wind increased, characteristic of an expansion fan. As a result, the Richardson number becomes reduced and favors shear instability that breaks down into turbulence. Observations indicate that a secondary well-mixed layer develops above the MBL that is bounded by narrow layers of high stability separating the secondary layer from the MBL below and the free troposphere above. It is hypothesized that the secondary layer develops as a result of Kelvin–Helmholtz instability, although more targeted observations are needed to confirm or reject that hypothesis.

1. Introduction

During the spring and summer, the near-surface wind along the California coast is typically from the northwest. A coastal low-level jet is often present with a distinct maximum of wind speed at the top of the marine atmospheric boundary layer (MBL). The MBL is characterized by cool, moist air underneath a marked temperature inversion, which separates the MBL from the warm, dry free troposphere aloft. Different aspects of this flow have been investigated through observational studies (e.g., Winant et al. 1988; Rogers et al. 1998; Dorman et al. 1999) and modeling studies (e.g., Samelson 1992; Burk and Thompson 1996; Rogers et al. 1998; Burk et al. 1999; Rogerson 1999; Tjernström and Grisogono 2000). The flow along the coast is forced by large-scale conditions consisting of a subtropical surface anticyclone over the Pacific Ocean (the Pacific high) and the thermal low over the desert southwest of the United States. These large-scale surface features produce a pressure gradient force that drives the northwesterly wind along the coast and there is large-scale subsidence over the region.

The coastal flow is modified locally by the topography of the coastline, which generally has an elevation comparable to or higher than the depth of the MBL. Given that the flow is bounded vertically by the inversion at the top of the MBL and laterally by the coastal topography, the dynamics of the flow is often interpreted in the context of hydraulic theory (e.g., Edwards et al. 2001; Haack et al. 2001). Hydraulic features such as compression bulges and expansion fans can occur when the Froude number is near or greater than unity. In this context, the Froude number is defined as the ratio of the mean flow in the MBL to the propagation speed of the

Corresponding author address: David A. Rahn, Department of Geography and Atmospheric Science, University of Kansas, 1475 Jayhawk Blvd., 201 Lindley Hall, Lawrence, KS 66045-7613.
E-mail: darahn@ku.edu

DOI: 10.1175/JAS-D-15-0363.1

© 2016 American Meteorological Society

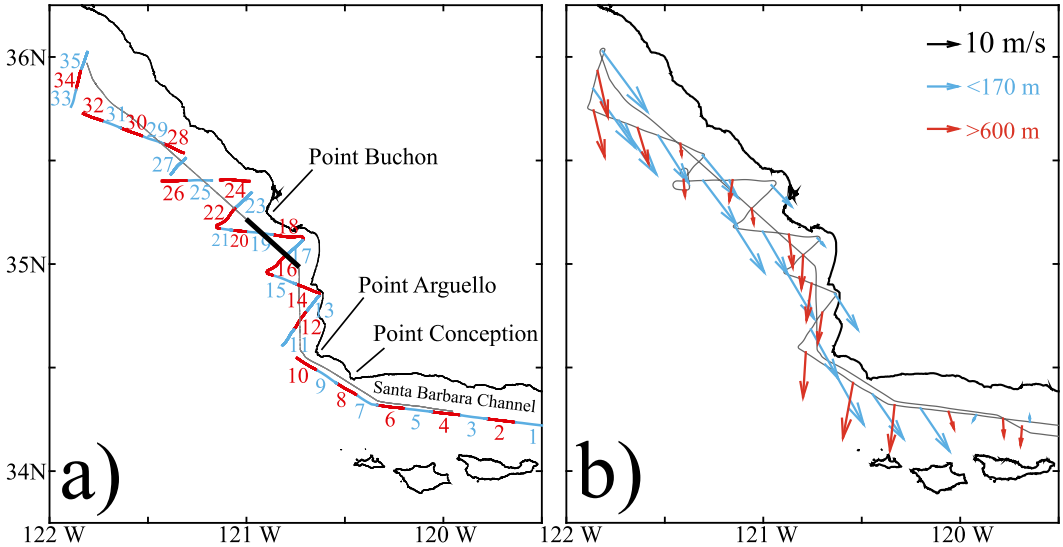

FIG. 1. (a) Locations of individual soundings with their corresponding number and the isobaric leg (gray line). (b) Observed resultant wind vectors for segments below 170 m (blue) and above 600 m (red).

fastest possible gravity wave within the MBL. If the fastest possible gravity wave travels more slowly than the mean flow, gravity waves cannot travel upstream and it is possible for discontinuities such as hydraulic jumps to manifest in the flow. Many examples of hydraulic features in the atmosphere have been observed (Winant et al. 1988), simulated in idealized models (Samelson 1992), and simulated in more complex models (Dorman and Koračin 2008).

The primary focus of many studies is on the near-surface wind response to changes in the coastline because of the impact on the coastal upwelling driven by the surface wind stress. Other studies examine what is happening above the MBL. For instance, Tjernström and Grisogono (2000) identify a single lee-wave pattern in the lee of Cape Mendocino that impacts the MBL depth and wind. Burk et al. (1999) examine the hydraulic response of the flow to a bend to the coastline using a mesoscale numerical model and shallow-water similarity theory based on Yih (1969). They find that the changes of the inversion height are similar between the mesoscale model and similarity theory, but the deformation of the isentropes above the MBL had only qualitative agreement and there was less agreement in the kinematic field.

Under the framework of the shallow-water layer response to changes in the lateral boundary, the upper level is often assumed to be a passive layer (e.g., Winant et al. 1988; Samelson 1992; Samelson and Lentz 1994). To a first approximation, the shallow-water theory explains most of the forcing and it is the essential component. As our understanding of the system has been refined, it has become difficult to ignore processes that are occurring aloft (e.g., Burk et al. 1999; Tjernström and Grisogono 2000). Several recent case studies in Southern California using aircraft observations and remote sensing measurements have been used to examine this aspect. Measurements of the lower atmosphere were obtained during the Precision Atmospheric Marine Boundary Layer Experiment (PreAMBLE)—a month-long field campaign from mid-May to mid-June 2012 that took place mainly in the vicinity of Point Conception (see Fig. 1a for locations).

The PreAMBLE flights resulted in a series of case studies highlighting different aspects of the forcing. Rahn et al. (2013) examined a case thought to be most representative in terms of conditions and forcing to the ideal setup often described in the literature. A large jump in the MBL height corresponded to changes in the wind over scales of tens of kilometers. The precise measurements allowed a direct comparison between what would be expected under an idealized scenario (channel flow analogy and Bernoulli's equation for inviscid flow) and the actual atmospheric response. Most of the response was associated with the rapid change in MBL height, but differences were attributed to other factors such as the change of inversion layer thickness or thermal gradients that existed above the MBL.

Parish et al. (2014) presented a case where the transition of the MBL around Point Arguello was strongly influenced by offshore flow. Several markers of the continental flow were present in not only the wind and temperature measurements but also the aerosol tracers. Aerosol concentrations increased by a factor of 2 just above the relatively clean MBL layer, indicating

offshore transport of continental aerosol above the MBL. The upward- and downward-looking lidars provided additional evidence with a high depolarization ratio indicating dry, irregularly shaped aerosols and, therefore, by extension, flow of continental origin.

Rahn et al. (2014) revealed how easterly flow coming from the Santa Barbara Channel can interact with the strong northwesterly flow from north of Point Conception. Lidar and in situ measurements indicated three distinct layers just southeast of Point Conception where the opposing flows met. Each layer contained alternating flow directions (northwesterly near the surface, southeasterly in the middle layer, and northwesterly aloft). In that case, a two-layer model was not sufficient to explain the dynamics.

Findings from those studies highlight the importance of other features beyond the essential components of hydraulic response of the MBL. This theme is continued here with the main objective of examining the conditions and implications of processes above the MBL near Point Buchon when particularly high wind speeds exist over a large segment of the Southern California coastline. The high wind shear associated with the low-level jet can lead to shear instabilities that profoundly impact the structure of the lower atmosphere.

2. Data sources

The University of Wyoming King Air was the primary observational platform in PreAMBLE. Unlike the other PreAMBLE studies that focus more on the transition of flow into the Santa Barbara Channel (Rahn et al. 2013; Parish et al. 2014; Rahn et al. 2014), the flight from 1417 to 1727 UTC on 24 May 2012 was designed to capture a broader stretch of the coastline, extending nearly to Monterey Bay. The strategy was to obtain many vertical profiles with the aircraft by repeatedly ascending and descending between ~150 and 640 m above the ocean surface. The upper and lower bounds of the sawtooth profiling were selected to ensure that the observations extended from within the MBL to above the inversion layer and core of the jet. The initial choice of level was based off of previous flights and did not require modification during the mission. This sawtooth pattern was conducted along the coast in linear segments at slightly different offshore positions and included soundings that entered the two bays surrounding Point Buchon. Note that, while the vertical profiles are presented as individual vertical soundings, a horizontal distance of about 11 km is traveled during each sounding as the aircraft ascends or descends. The return leg back to the base of operations at the Naval Air Station at Point Mugu, California, was flown at a constant isobaric level of 981 hPa. The along-leg pressure gradient force can be inferred from the change of aircraft height while flying on the isobaric surface. The error range of the primary measurements are 0.5°C for temperature, 1 m s^{-1} for horizontal velocity, 0.15 m s^{-1} for vertical velocity, and 0.5 hPa for static pressure. For brevity, we refer to Parish et al. (2007) and Parish and Leon (2013) for more details regarding the aircraft instrumentation and techniques.

Along with the suite of in situ measurements described in Parish et al. (2014), the UWKA also carried the Wyoming Cloud lidars (WCLs)—a pair of 355-nm lidars designed for retrieval of cloud and aerosol properties. One of the WCLs was pointed upward and the other downward. Details of the WCLs can be found in Wang et al. (2009) and Z. Wang et al. (2012). The primary role of the WCLs in this application is to detect sharp gradients in attenuated backscatter and linear depolarization ratio to identify distinct layers in the atmosphere. The top of the well-mixed MBL is easy to detect in the lidar returns but other more subtle layering, crucial to the interpretation of processes occurring above the MBL, is also evident in the MBL data.

Since the most important wind components are relative to the coastline, the zonal and meridional wind components are projected onto new axes and become the alongshore and cross-shore wind components. The orientation of the coastline is defined as 33° west of north (along 327°), as is commonly used in other studies (e.g., Veneziani et al. 2009). Thus, a positive cross-shore wind is onshore and a positive alongshore wind is toward the north-northwest.

3. Results

a. Overview

Nearly all of the area where the flight occurred was cloud free. A low-level pressure gradient associated with an anticyclone that was considerably stronger than the May average (Fig. 2a) was present near the coast. Alongshore wind in excess of 14 m s^{-1} was reported at 1500 UTC 24 May 2012 from WindSat analyses (Gaiser et al. 2004), buoys,[1] and surface stations along the coast (Fig. 2b). The wind produced a particularly rough ocean surface on this day that was clearly noticeable from the aircraft.

Wind measurements from the aircraft also indicate a strong alongshore wind near the surface. Resultant winds in the segments of the sawtooth profiling below 170 m (Fig. 1b) show an alongshore direction. A sense of the

[1] No wind reports from buoy 46011 on this day.

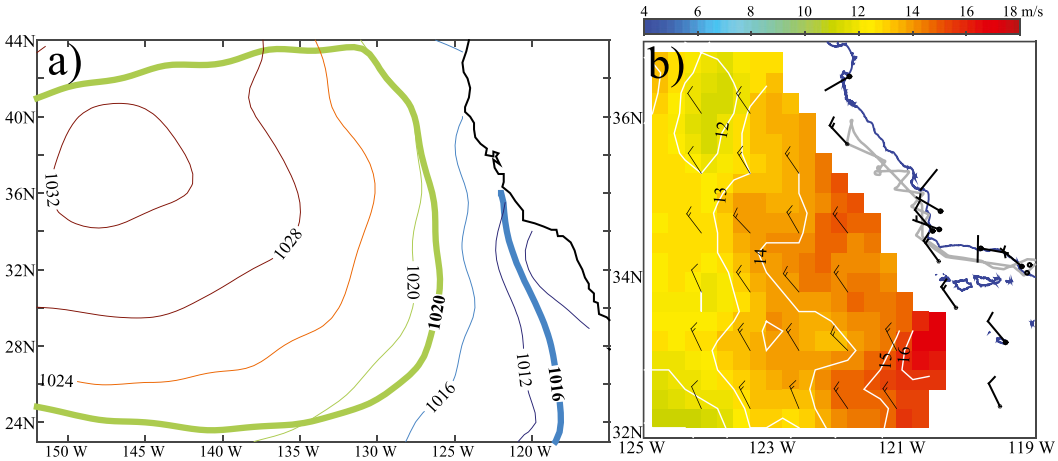

FIG. 2. (a) The average sea level pressure from the Climate Forecast System Reanalysis (Saha et al. 2010) for May 1979–2014 (thick contours, every 4 hPa) and the 1200 UTC 24 May 2012 sea level pressure (thin contours, every 4 hPa). (b) Inferred 10-m wind at 1448 UTC from WindSat (colors and thin wind barbs, m s^{-1}) and 1500 UTC wind barbs from buoys and surface coastal stations (thick wind barbs, m s^{-1}).

vertical wind shear along the coast is obtained by comparing winds at the bottom of the sawtooth profile with those at the top (above 600 m). Wind directions near the bottom of the sawtooths typically follow the coastline, while at the peak of the sawtooth the wind tends to be more northerly with some offshore component.

b. Northern conditions

Beginning with the upstream conditions in the northern section, soundings 28–35 reveal the typical well-mixed MBL capped by a temperature inversion. Sounding 31 exemplifies features in the northern segment (Fig. 3). The temperature profile in the MBL is nearly dry adiabatic, indicating that the layer is well mixed. The top of the well-mixed layer is near 330 m and the magnitude of the temperature inversion is about 5°C. The observations depict a sharp temperature inversion over a depth of about 50 m that becomes essentially isothermal up to 650 m. A large moisture gradient is likely related to subsidence of dry air above the inversion and the high static stability associated with the large temperature gradient that inhibits mixing through the temperature inversion.

Wind speed reaches a maximum of 25 m s^{-1} at the base of the inversion and decreases rapidly with height. The dominant wind component is in the alongshore direction. The observed cross-shore wind is weak and transitions from 1–2 m s^{-1} directed onshore within the MBL to about 4 m s^{-1} offshore at the top of the profile where the alongshore component has reduced to 10 m s^{-1}. Thus, toward the top of the profile the offshore wind becomes more apparent as indicated in Fig. 1b. Other soundings in this segment are similar to sounding 31.

The WCL provides a more continuous view of the MBL structure along the straight segment to the northwest comprised of soundings 28–32 (Fig. 4). The MBL top is marked by the large vertical gradient in the backscatter and depolarization ratio around 300 m. The lidar returns indicate a single, well-defined layer at this location. The greatest slope of the top of the MBL along the flight leg is on the southeast end that is closest to the coast. Higher values of attenuated backscatter indicate higher aerosol concentration or larger aerosol that is most likely deliquesced at the top of the MBL where the relative humidity is the greatest. Deliquesced aerosols are consistent with the observed low depolarization ratio. An interpolated cross section (Fig. 5) of the sawtooth pattern along the entire northern segment, soundings 28–35 and including the change of heading between soundings 32 and 33, reveals that the alongshore wind is generally strong (>20 m s^{-1}) and decreases slightly toward the southeast. A fairly uniform offshore flow exists above the MBL layer with some onshore flow within the MBL. While soundings 28 to 35 are generally taken in an alongshore direction, the soundings closest to the coast (28 and 35) reveal that the depth of the MBL decreases toward the coastline.

An important diagnostic for the low-level flow is the Froude number (Fr). Similar to Dorman and Koračin (2008), it is defined here as

$$\mathrm{Fr} = \frac{U}{\sqrt{g\dfrac{\theta_t - \theta}{\theta}H}}, \tag{1}$$

where U is the average wind speed in the MBL, g is the acceleration of gravity, θ_t is the potential temperature at

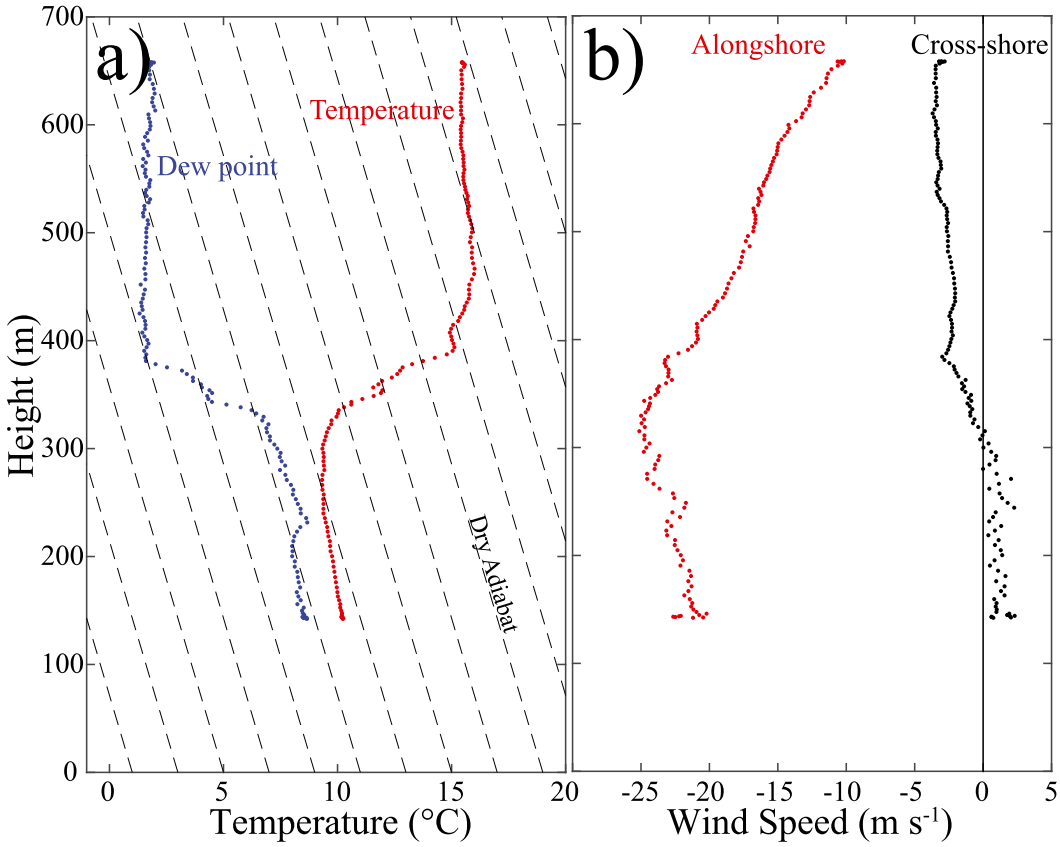

FIG. 3. Sounding 31. (a) Temperature (°C, red), dewpoint temperature (°C, blue), and dry adiabats (dashed black line). (b) Alongshore (red) and cross-shore (black) wind components (m s^{-1}).

the top of the inversion, θ is the average potential temperature in the MBL, and H is the depth of the MBL. Using characteristic values of the northern soundings of $U = 20\,\mathrm{m\,s^{-1}}$, $H = 350\,\mathrm{m}$, $(\theta_t - \theta) = 5\,\mathrm{K}$, and $\theta = 285\,\mathrm{K}$, the Froude number is 2.5, which is well into the supercritical range. Since the Froude number is derived from ideal conditions, its meaning is not as precise in the real atmosphere (Burk and Thompson 1996). Nevertheless, it provides us with a tool to determine if hydraulic features are likely to manifest in the flow or not. In fact, transcritical regimes of the Froude number that fall between 0.5 and 1 can often exhibit hydraulic features (Rogerson 1999). High wind speed and an MBL depth that is at or lower than 350 m are found all along the coast during this flight. As a result, the flow within the MBL in each of the following soundings is considered to be in the supercritical range.

c. *Profile above the MBL*

Sounding 27 is a single descent between the longer series of profiles to the north and a zonal set of profiles to the south (Fig. 6). While at first glance the sounding looks fairly similar to the other northern soundings, a peculiar layer is present near 500 m that gives clues to features that exist just above the MBL. Comparing the lapse rate of this approximately 50-m-deep layer to the dry adiabatic lapse rate, it appears to be superadiabatic. The feature could be due to an instrument error, but this is not likely. Two temperature sensors, a standard Rosemount 102 sensor and a reverse flow temperature sensor, are maintained on board the aircraft. The reverse flow temperature has the sensor shielded in a housing where the air flows in a direction opposite to the airstream—intended to reduce the wetting or icing of the sensor (Rodi and Spyers-Duran 1972). Reverse flow temperature sensor data is used in all plots. Data from the reverse flow and also the Rosemount sensor are plotted in Fig. 7a. While there is a slight warm bias in the reverse flow sensor when compared to the standard Rosemount 102 sensor, the apparently superadiabatic slope of the temperature profile is essentially the same. Thus, instrument error can be ruled out.

The sounding is not strictly vertical so some horizontal temperature gradient could contribute to this profile. Evidence of horizontal variations was sought from the WCL (Fig. 8a). The top of the MBL is clearly visible, but

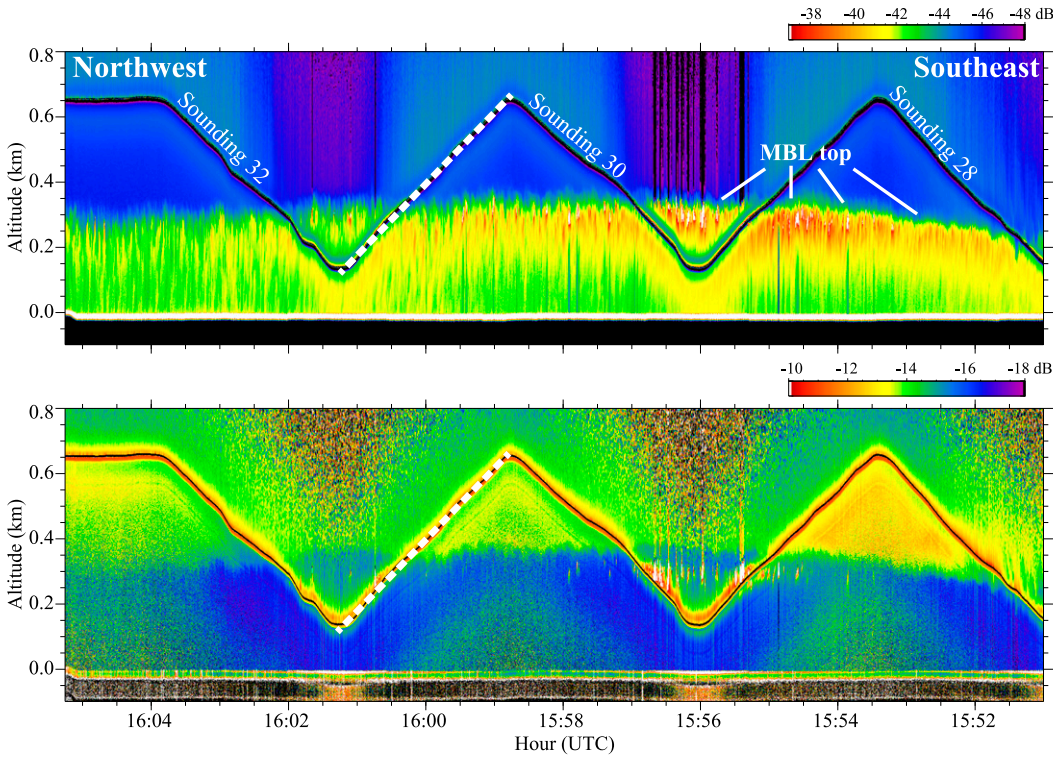

FIG. 4. Lidar returns of (top) uncalibrated attenuated backscatter and (bottom) uncalibrated depolarization ratio (dB) over soundings 28–32. Aircraft elevation is indicated by the black line and sounding 31 is indicated by the dashed white line.

no vertical gradient of backscatter or the depolarization ratio (not shown) is evident above the MBL. Beneath the observations taken around 500 m near the apparently superadiabatic layer, the top of the MBL exhibits depth variations with a wavelength of about 1.5 km. If the path of the aircraft is not orthogonal to the wave front (along the wave vector), then the actual wavelength may be shorter. Assuming that this perturbation extends upward, the flight path would intersect the wave feature as depicted in Fig. 8a. Thus, the small-scale horizontal gradient associated with a wave could explain the anomalous layer.

To investigate the possible role of a horizontal temperature gradient, a cross section of potential temperature is inferred from the sounding and lidar backscatter (Fig. 8b). A background vertical potential temperature gradient of 0.022 K m^{-1} is determined from the mean lapse rate just above and below the anomalous layer (Fig. 7d). A sine wave perturbation of potential temperature is embedded in the cross section with a wavelength of 1.5 km, corresponding to the wavelength in the lidar backscatter. The amplitude is set as 1.2 K, corresponding to a 55-m vertical displacement of the background potential temperature gradient of 0.022 K m^{-1}. The 55-m vertical displacement is slightly larger than that seen in the lidar backscatter, but it is a reasonable value. Also shown in Fig. 8b is the slope of the aircraft that is approximately 75 m km^{-1}. A comparison between the observed potential temperature along the sloped flight track and the constructed cross section (Fig. 8c) reveals that the horizontal gradient associated with the inferred wave is likely responsible for the anomalous layer.

Other aircraft measurements also indicate a sharp change. The wind speed above and below the anomalous layer decreases with height at a nearly linear rate of ~6 m s^{-1} every 100 m (Fig. 7b). This average wind shear could be extended all the way from the core of the low-level jet to just above the anomalous layer, even though the wind speed in the anomalous layer is constant. The carbon dioxide (CO_2) concentration also shows a strong anomaly in the layer (Fig. 7c). As expected, the CO_2 concentration in the MBL is uniform because the CO_2 has been well mixed by the persistent turbulence. Above the inversion, CO_2 concentrations tend to linearly decrease with height until reaching the anomalous layer. A local minimum in CO_2 occurs at the bottom of the layer and a local maximum occurs at the top.

In the anomalous layer there is a change of peak vertical wind speed from about −0.5 to +0.4 m s^{-1}

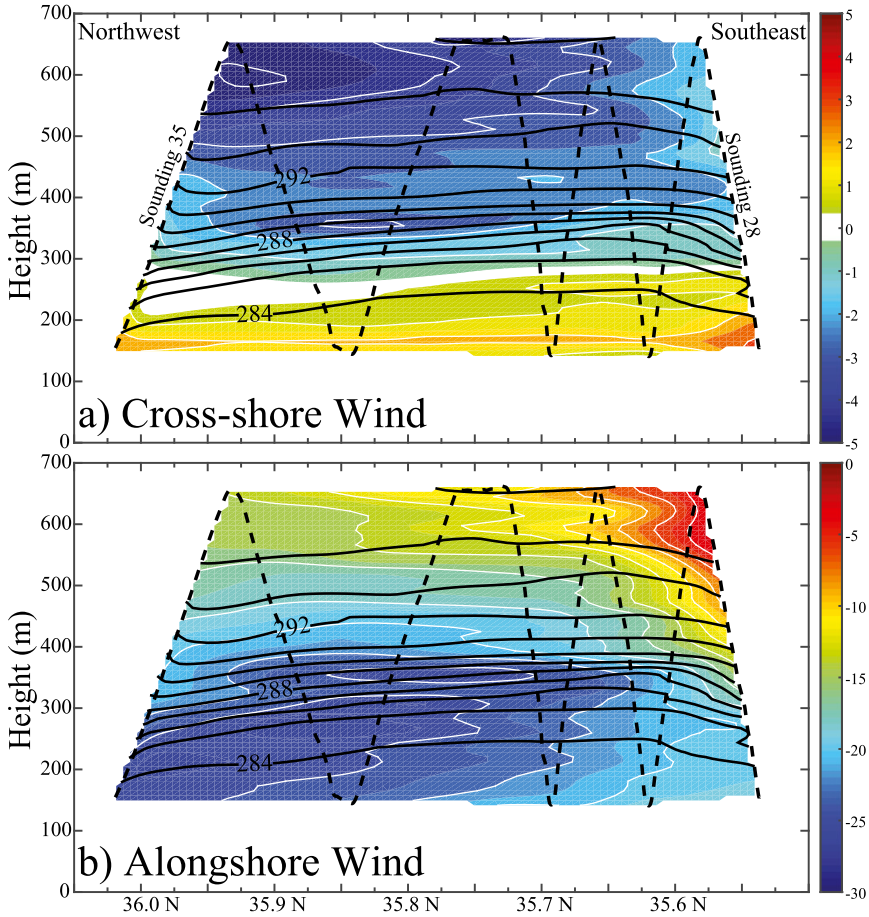

FIG. 5. Cross section of soundings 28–35. Flight track indicated by the thick dashed line. The potential temperature (K, black lines) and the (a) cross-shore and (b) alongshore wind ($m\,s^{-1}$, color scale) are interpolated between soundings. Note there are different color scales.

(Fig. 7e). The change in vertical motion of about $0.9\,m\,s^{-1}$ over ~1 km could be a sign of going through a coherent structure. It is interesting to note that the largest observed downward motion at 500 m is associated with the cold potential temperature anomaly and that upward motion at 425 m is associated with the warm potential temperature anomaly. This would be consistent with vertical motion driven by buoyancy.

A proxy for turbulence is given by the measurement of the eddy dissipation rate (EDR) using the method developed by MacCready (1964), which relates gust loads on an aircraft to the EDR. On board the aircraft is the Meteorology Research Incorporated's Universal Indicated Turbulence System (MRIUITS). The MRIUITS estimates the EDR from the root-mean-square of the signal from the pitot tube by assuming a $-5/3$ slope of the energy spectrum within the inertial subrange and local isotropy. The estimate from the pitot tube agrees to within 5% when the full three-dimensional winds from the gust probe are used (Feng 2001). More recently, Strauss et al. (2015) compared the EDR measurement from the MRIUITS and the log-mean EDR estimate that uses each wind component (u, v, and w), and they also found very good agreement, but the measurements were not reliable at low values. EDR has become the standard metric in civil aviation for atmospheric turbulence (Sharman et al. 2014).

Higher values of the EDR indicate greater turbulence. The entire profile indicates generally modest turbulence with EDR values around $0.1\,m^2\,s^{-3}$ (Fig. 7f). A moderate spike in turbulence occurs near the warm potential temperature anomaly at the bottom of the anomalous layer with peak values near $0.2\,m^2\,s^{-3}$. This is collocated with a high amount of wind shear that would be responsible for the mechanical generation of turbulence.

The most plausible explanation for the anomalous layer is the horizontal variation associated with the wavelike feature inferred from the top of the MBL. Given the presence of a wave perturbation indicated by

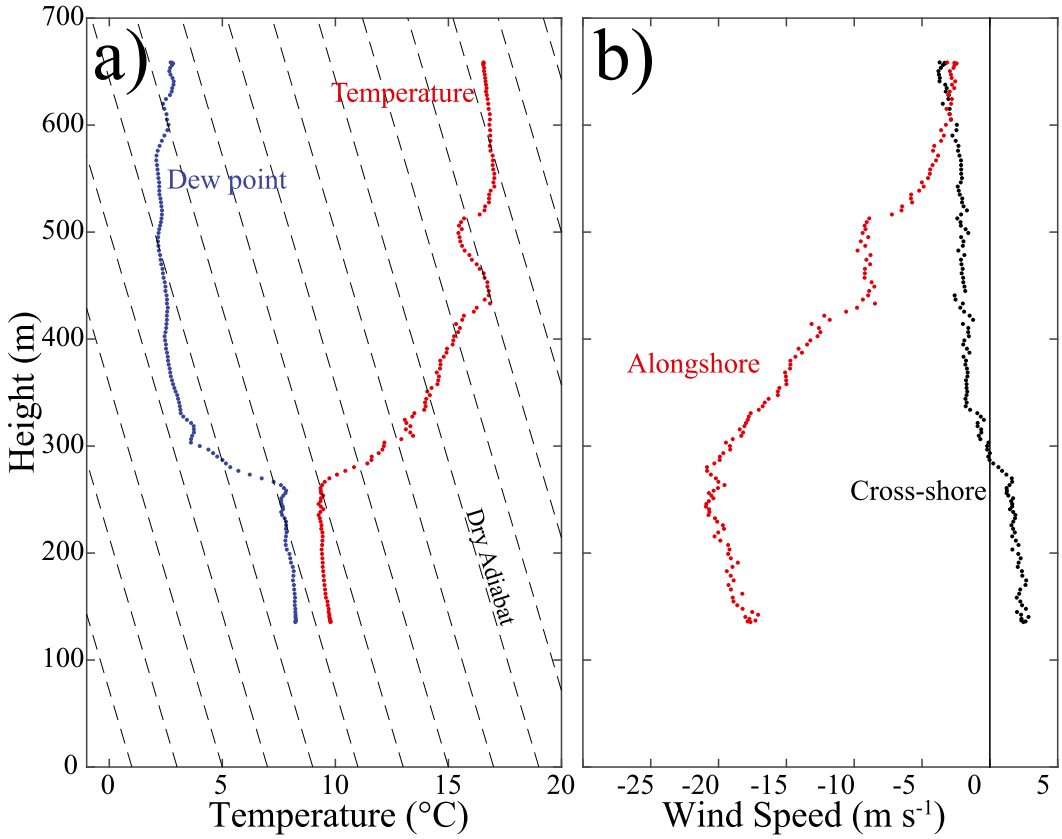

FIG. 6. As in Fig. 3, but for sounding 27.

the lidar returns in Fig. 8a that is likely to extend upward and the high vertical wind shear seen in Fig. 6, Kelvin–Helmholtz instability (KHI) is introduced now and then further explored at locations downstream of sounding 27. The bulk Richardson number (Ri_b; e.g., Stull 1988) is used to quantify the ratio of thermal stability to vertical wind shear:

$$\mathrm{Ri}_b = \frac{g}{\overline{\theta}_v}\frac{\Delta\theta_v \Delta z}{(\Delta U)^2}, \tag{2}$$

where $\overline{\theta}_v$ is the layer average virtual potential temperature, $\Delta\theta_v$ is the difference in virtual potential temperature in the layer, Δz is the layer thickness, and ΔU is the difference of wind speed in the layer. Large values of Ri_b indicate high thermal stability and small wind shear that is associated with less turbulence, and small values of Ri_b indicate low thermal stability and large wind shear that is associated with more turbulence. Note that above the MBL the only appreciable vertical wind shear is in the alongshore direction and there is little cross-shore wind or cross-shore wind shear (Fig. 6b).

Any time that observations are used in conjunction with theory, the results are subject to issues such as the selection of representative layers for the observations or violation of the underlying assumptions. Nevertheless, it is a worthwhile comparison that provides a basis for making conclusions about the physical processes occurring in the atmosphere. The 400- and 550-m levels are chosen to be the upper and lower bounds of the layer above the MBL. That layer represents the mean conditions above the MBL and contains the anomalous layer. With the exception of the anomalous layer itself, the virtual potential temperature gradient and wind shear in the vicinity of that layer are fairly uniform. Over that 150-m layer, ΔU is 8.6 m s^{-1}, $\Delta\theta_v$ is 3.3 K, and $\overline{\theta}_v$ is 294 K, which yields a Ri_b of 0.22.

Under strictly linear theory assuming horizontal, steady, and nondiffusive flows, a Ri_b that is greater than 0.25 indicates that the stratified shear flow is stable to small disturbances (Howard 1961; Miles 1961). Under this specific framework, KHI is possible when the value drops below a critical Ri_b of 0.25, but it is not guaranteed since a low Ri_b is a necessary but not sufficient condition for KHI. This means that the layer does not need to become unstable, but it is at least a possibility. A linear stability analysis only really applies at the onset of an instability and does not describe the subsequent development.

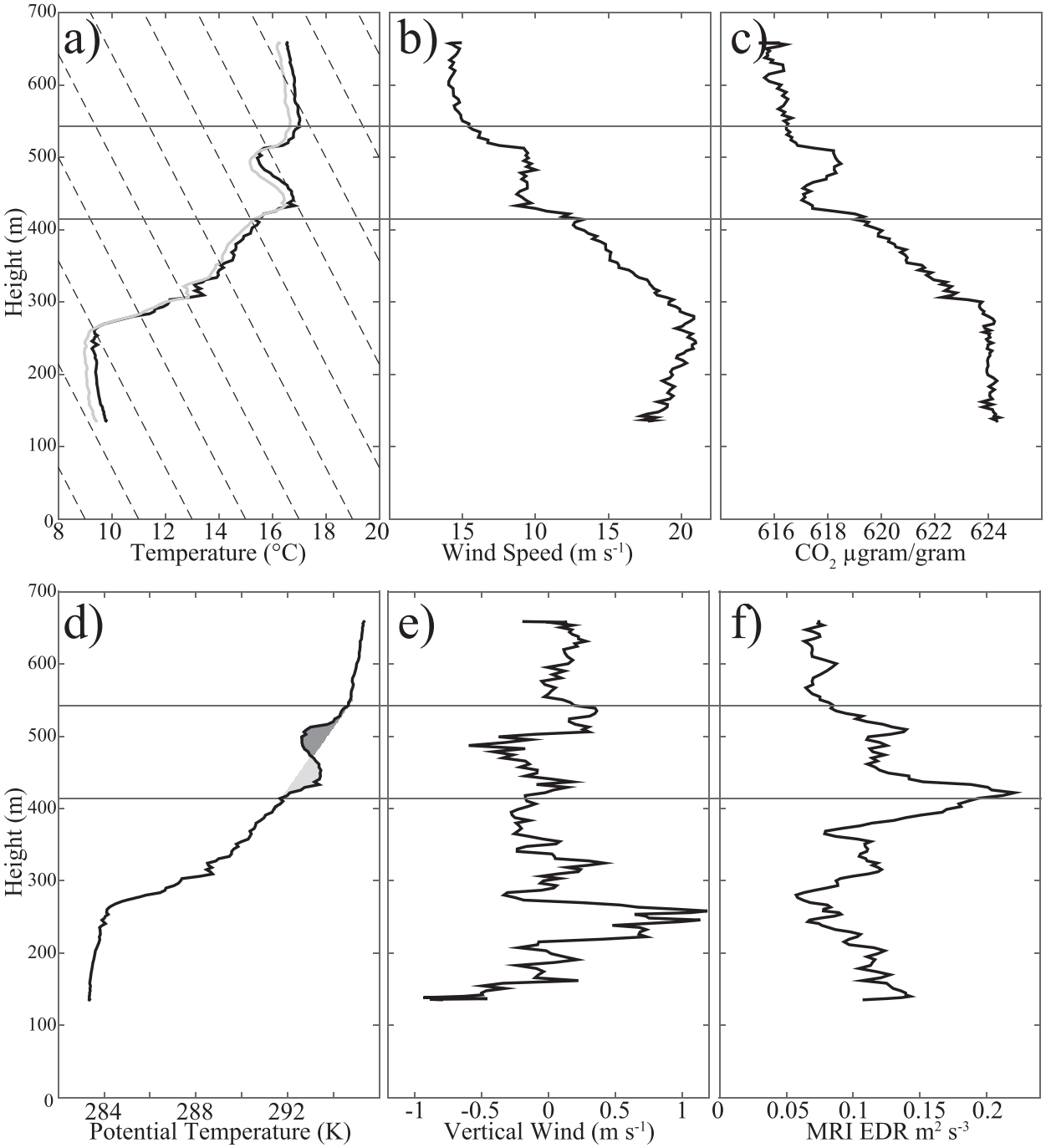

FIG. 7. For sounding 27, (a) dry adiabats (dashed), reverse flow (black), and Rosemount 102 temperature (gray, °C); (b) wind speed ($\mathrm{m\,s^{-1}}$); (c) carbon dioxide concentration ($\mu\mathrm{g\,g^{-1}}$); (d) potential temperature (K) with warm and cold anomalies shaded light and dark, respectively; (e) vertical wind speed ($\mathrm{m\,s^{-1}}$); and (f) EDR ($\mathrm{m^2\,s^{-3}}$). Horizontal lines through all soundings indicate the anomalous layer.

Subsequent studies have revealed that the relationship between the Ri_b and KHI is more complicated than the simple 0.25 threshold derived from an idealized framework. For example, Smyth and Peltier (1989) demonstrated that KHI exists for Ri_b substantially greater than 0.25. Troy and Koseff (2005) examine the breaking of long internal waves by using a wave-induced gradient Richardson number that incorporates the wave steepness. They find that as the wavenumber increases, the critical wave Richardson number decreases. From

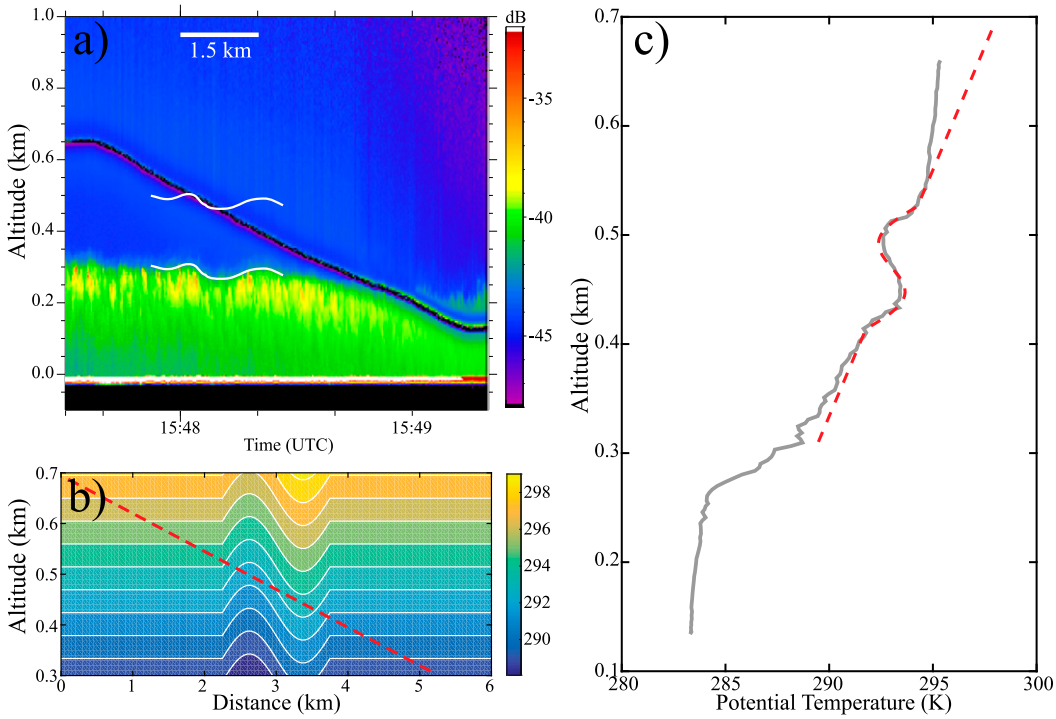

FIG. 8. (a) Lidar returns of uncalibrated attenuated backscatter (dB) during sounding 27. Aircraft elevation is indicated by the black line. The lower white line is the approximate height of the boundary layer and the upper white line is the inferred variation near the anomalous layer. (b) Inferred distribution of potential temperature (K) in the cross section (details given in the text) and the slope of the flight track (red dashed). (c) The profile of potential temperature during the sounding (gray) and the profile of potential temperature given both the assumed distribution of potential temperature in (b) and the slope of the flight track (red dashed).

the preceding studies, it is clear that outside of the most ideal models there is no single threshold that determines dynamic instability. In fact, representation of turbulence in numerical simulations is moving away from the concept of a critical Ri_b and toward formulations that are valid over a range of Ri_b (e.g., Grisogono and Belušić 2008; Ďurán et al. 2014). Formulations such as in Zilitinkevich et al. (2007) result in a transitional Ri_b between 0.1 and 1 that separates the strong turbulence regime at low Ri_b and the weak turbulence regime at high Ri_b. Thus, the concept of a single critical Ri_b derived from classical derivations is in reality better represented as a continuum.

Although in the real atmosphere deviations from any idealized theoretical framework make a direct comparison imprecise, it is possible to at least estimate other characteristics of the KHI from simple linear models such as that developed in Scorer (1969). Since there is a wave detected at the top of the MBL by the WCL, the wavelength can be compared to the critical wavelength for KHI (λ_{crit}), which marks the wavelength between the linearly unstable wavelengths at shorter wavelengths and the linearly stable wavelengths at longer wavelengths:

$$\lambda_{\mathrm{crit}} = \frac{\pi\overline{\theta}_v}{g}\frac{(\Delta U)^2}{\Delta\theta_v}. \tag{3}$$

Similar to how Ri_b is better represented as a continuum rather than a single threshold, the simple framework used to derive Eq. (3) (Scorer 1969) can be modified to arrive at slightly different values. For example, Cushman-Roisin (2005) approaches the problem as a boundary layer problem and finds the following relationship:

$$\lambda_{\mathrm{crit}} = \frac{\pi\overline{\theta}_v}{g}\frac{(\Delta U)^2}{\Delta\theta_v}\left[1 + \frac{u_1 + u_2}{\sqrt{2(u_1^2 + u_2^2)}}\right]^{-1}. \tag{4}$$

Thus, similar to Ri_b, the λ_{crit} is better thought of as a range with smaller wavelengths more likely to be unstable and larger wavelengths likely to be stable. These idealized derivations are used as a benchmark to assess the dynamics, but it is recognized that they are not exact expressions of the real atmosphere. The simple relationship in Eq. (3) has been used elsewhere in observational studies of KHI in the upper troposphere (e.g., Browning and Watkins 1970). Using the values listed

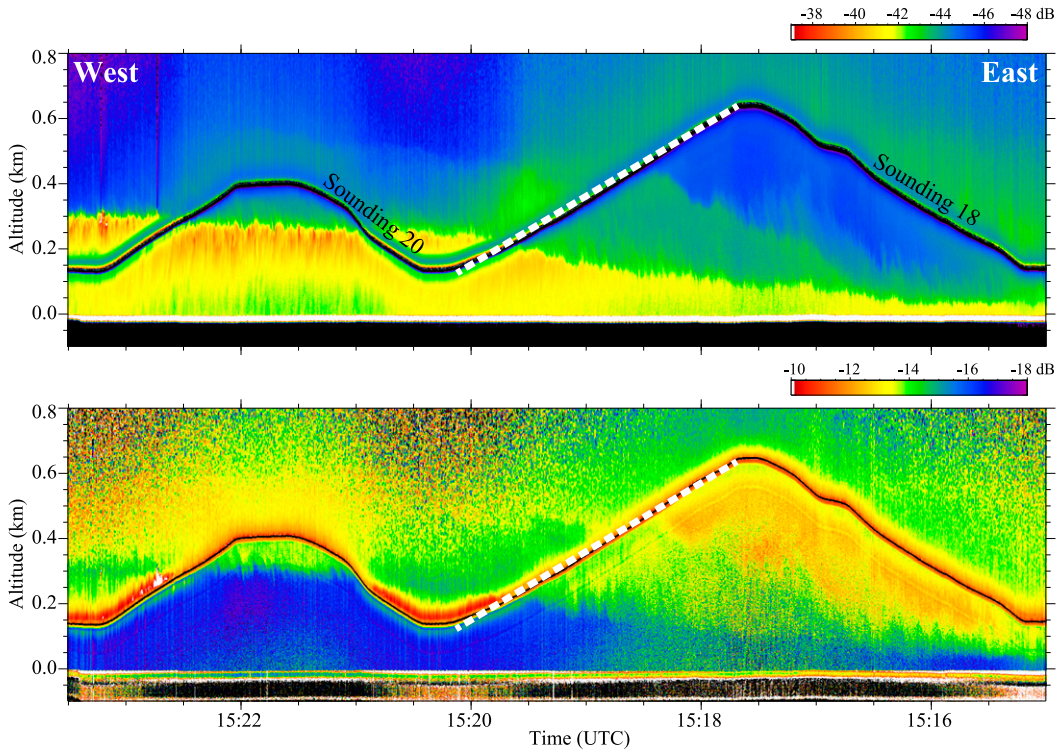

FIG. 9. As in Fig. 4, but for soundings 18–21. Sounding 19 is indicated by the dashed white line.

above, the λ_{crit} is 2.1 km from Eq. (3) and 2.2 km from Eq. (4). Again, assuming that the wave pattern seen at the top of the MBL extends upward with approximately the same characteristics, the observed wavelength would be ~1.5 km, which would also indicate that instability is a possibility. In fact, the wavelengths that have the fastest growth rates are about half of λ_{crit}. In general, the vertical wind shear increases southward from the upstream soundings (Figs. 3b and 5b) toward Point Buchon. At sounding 27, a low Ri_b suggests that it is not unreasonable to have KHI, which may have an impact further downstream.

d. Point Buchon

Another sequence of soundings (18–21) was taken along a nearly zonal track near Point Buchon where the topography exerts a greater influence. Since this flight segment enters the bay south of Point Buchon and is directed more perpendicular to the coastline, signs of hydraulic features associated with supercritical flow ($Fr > 1$) are expected. Backscatter from the lidar (Fig. 9) reveals that the MBL depth descends from 350 m offshore to nearly down to the surface at the eastern end of the flight segment. The large change in MBL depth suggests the existence of an expansion fan. A secondary layer of moderate backscatter above the MBL is clearly evident in the vicinity of sounding 19. The aircraft passes through another large vertical gradient of backscatter near a height of 400 m. The greatest alongshore wind, and presumably vertical wind shear, should be encountered near the top of the MBL between 1517 and 1520 UTC, which is also linked to the base of the secondary layer of high backscatter.

Examining the in situ measurements of sounding 19 (Fig. 10), the alongshore wind speed reaches 17 m s^{-1} near a height of 200 m, which is at the top and western edge of the steeply sloped MBL (Fig. 9). A narrow layer of high stability caps the well-mixed MBL near 225 m, but above the MBL there is a layer of low stability capped by another layer of high stability near 450 m. These narrow layers of high stability coincide exactly with the layers evident in the lidar returns. In situ measurements show that the middle layer is well-mixed since the potential temperature is nearly constant and mixing is promoted by the moderate turbulence observed in the layer as indicated by the EDR.

Aerosol and CO_2 concentrations (Figs. 10c,d) in the middle layer also support the existence of a well-mixed layer. In fact, these measurements reveal that a large amount of mixing is occurring through the MBL and into the middle layer, indicating exchange through the lower inversion (i.e., top of the MBL). The gradient of aerosol concentration and CO_2 mixing ratio across the stronger upper inversion indicates less entrainment. An

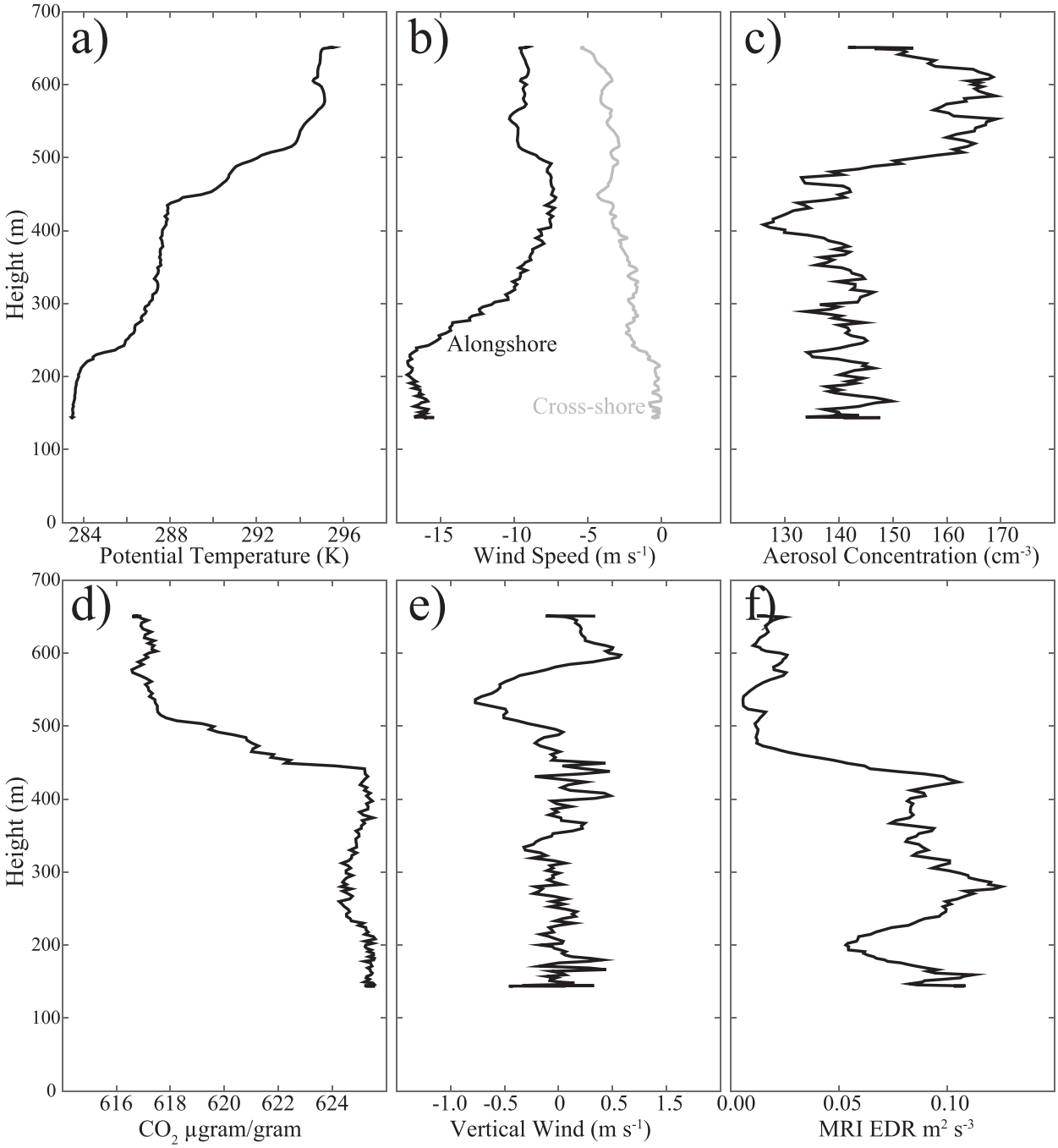

FIG. 10. For sounding 19, (a) potential temperature (K), (b) alongshore (black) and cross-shore (gray) wind speed ($m\,s^{-1}$), (c) aerosol concentration (cm^{-3}), (d) carbon dioxide concentration ($\mu g\,g^{-1}$), (e) vertical wind speed ($m\,s^{-1}$), and (f) EDR ($m^2\,s^{-3}$).

increase of aerosol concentration and an offshore wind component in the upper layer is consistent with advection of fine aerosol off the continent. Other evidence of offshore flow is the confined layer of subsidence near 550 m as the flow descends off of the continent, which contributes to the increase of potential temperature in addition to warm air advection from the continent. These factors help explain why the upper stable layer has a greater stability than the lower stable layer and why less entrainment occurs across the interface between the upper and middle layers.

Signals of continental influence are clearest above 500 m with little evidence of continental influence below. While continental influence on the middle and

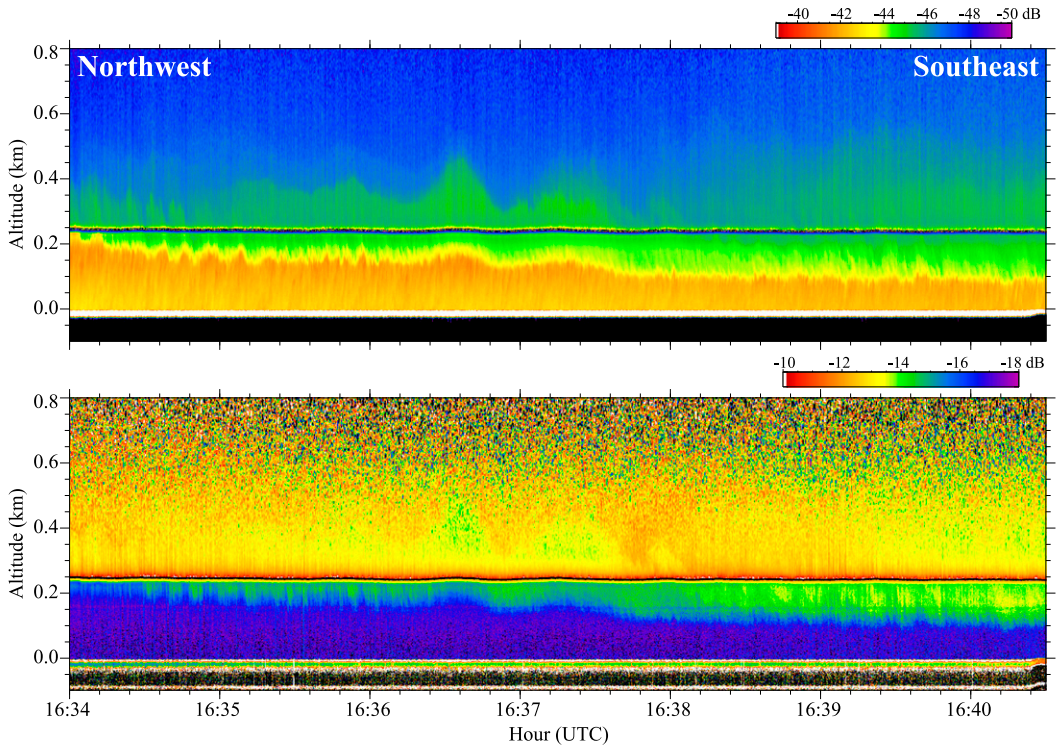

FIG. 11. As in Fig. 4, but for the 981-hPa isobaric leg near Point Buchon indicated by the thick black line in Fig. 2.

lower layers cannot be ruled out entirely, KHI is most likely the dominant factor in developing and maintaining the well-mixed middle layer bounded by two stable layers. The segment of the return isobaric leg near sounding 19 (thick black line in Fig. 2) is examined to help understand the variation in the alongshore direction. This flight leg is oriented nearly alongshore at a heading of 135°. Although these observations are taken over an hour after sounding 19, some indication of key features and processes at work should be present.

The lidar reveals that the depth of the MBL along the isobaric flight track decreases toward the south from 250 to 100 m (Fig. 11). Once again, a middle layer above the MBL and below the free troposphere is present. The top of this middle layer as inferred from the vertical gradient of reflectivity is well defined in the middle of the flight segment and somewhat more diffuse on either end. At a flight level of about 250 m, most of the in situ observations are taken just above the MBL. A conspicuous feature is the wave in the middle of the leg spanning ~11.3 km (from 1636 to 1638 UTC), which is evident in both the backscatter and also the depolarization ratio. It reaches an altitude nearly double that of the MBL depth. It is also evident that features collocated with this wave tend to be smoother than to the north and south.

Since the aircraft is flying along a constant pressure level (981 hPa), the height of the isobaric surface can be inferred (Fig. 12a). The wave pattern seen in the lidar image corresponds to the wave pattern in isobaric height that is embedded within the general downward slope of the isobaric height from north to south. A 4-m change of isobaric height is seen between the greatest peak and trough of the wave, which are separated by a horizontal distance of 1.5 km for a wavelength of 3 km. The isobaric height measurements appear slightly smoother within the large coherent wave structure than the noisier signal on either side.

The difference in smoothness is even more apparent in other in situ measurements. Away from the smoother signal near the large waves, the alongshore wind contains rapid variations on the order of 2–3 m s^{-1} while the temperature fluctuates by about 1°C. The vertical wind speed oscillates rapidly in the north and south ends of this leg, but only a large coherent wave pattern of vertical motion is present in the center that is within less turbulent flow. The EDR clearly indicates a minimum in turbulence near the center of the leg. Low turbulence in the middle of the leg and higher turbulence on either end are consistent with the difference in the high-frequency fluctuations of the in situ measurements.

Although it is difficult to definitively identify the reason for changes to turbulence of the alongshore flight leg, the observations are consistent with the idea that near the expansion fan in the northwest, the wind shear

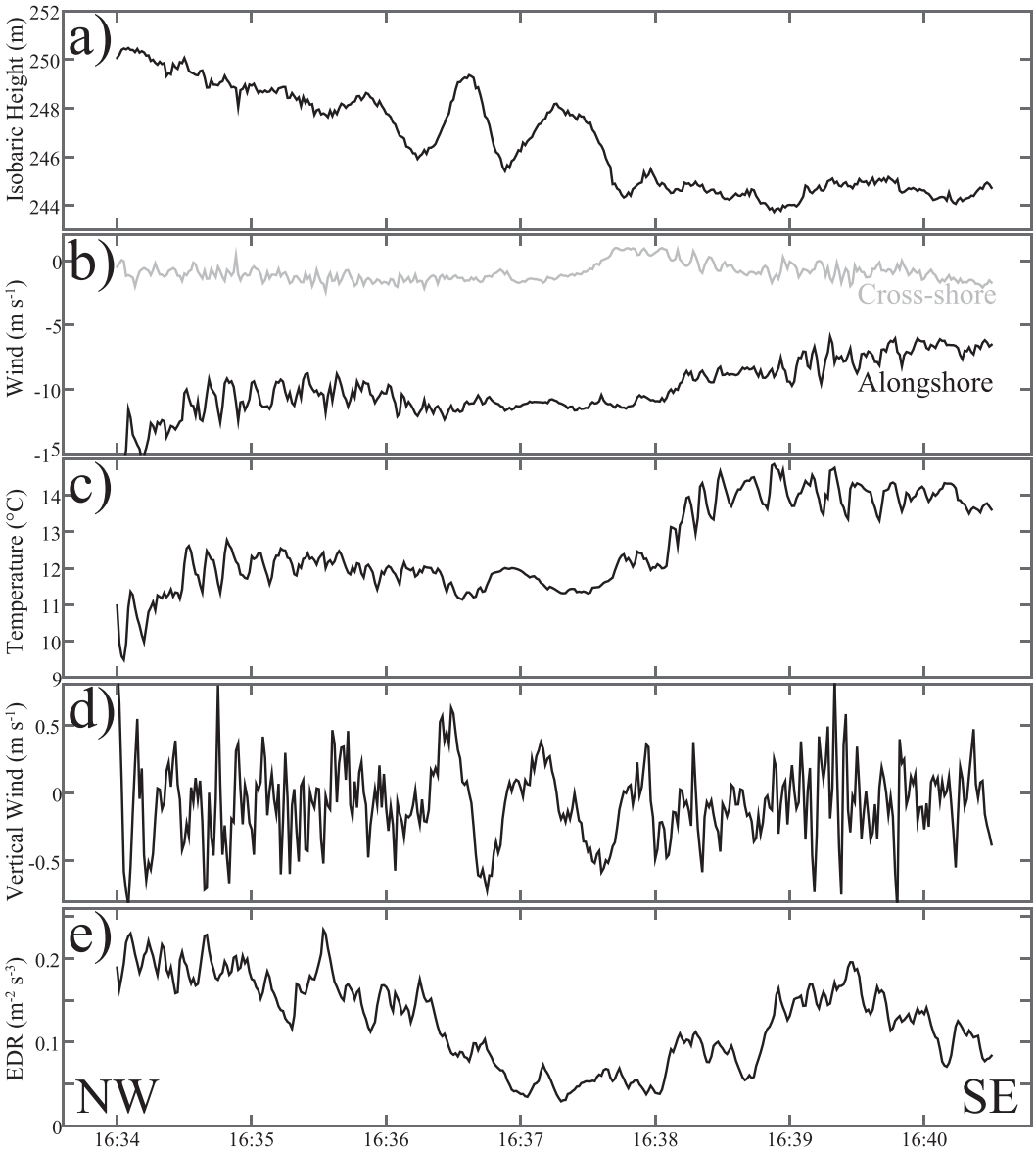

FIG. 12. Measurements along the 981-hPa isobaric leg near Point Buchon showing (a) isobaric height (m), (b) alongshore (black) and cross-shore (gray) wind speed (m s^{-1}), (c) temperature (°C), (d) vertical wind speed (m s^{-1}), and (e) EDR ($m^2 s^{-3}$). Northwest is to the left and southeast to the right. Time (UTC) is indicated along the *x* axis.

increases at the top of the MBL and overcomes the stability. Relatively small-scale turbulent structures seen in the lidar upstream toward the north eventually give way to less turbulent, larger, and more coherent structures toward the middle of the flight segment. The transition reflects the breakdown of the initial turbulent overturning into smaller eddies that dissipate the energy into smaller-scale turbulent motions downstream producing a well-mixed layer in the middle, which is reflected in the decrease of EDR at flight level and by the lidar returns above and below the aircraft.

At flight level the wind is alongshore. If the wind profile is similar to the sounding taken an hour previously, there must be substantial alongshore vertical wind shear. The measurements during the isobaric leg are obtained in the inversion layer just above the MBL or near the bottom of the middle layer. Using sounding 19 to represent the conditions near the middle of the isobaric leg, wind shear in the layer between 200 and 350 m is fairly constant near 6 m s^{-1} $(100\,m)^{-1}$. The lapse rate of potential temperature in the layer between 240 and 320 m is fairly constant near 2 K $(100\,m)^{-1}$ and in the

narrow layer between 210 and 240 m it is near 7 K $(100\,\mathrm{m})^{-1}$. The 210–240-m layer corresponds to a Ri_b of 0.67, and the 240–320-m layer corresponds to a Ri_b of 0.19. The higher Ri_b in the lower layer means that the mechanically generated turbulence from vertical wind shear is more likely to be suppressed by the stability than in the upper layer were the Ri_b is smaller. It is emphasized that these calculations are estimates and that the isobaric leg and sounding were taken an hour apart in a system that is likely to be constantly evolving.

Using the shear and stability values of the 240–320-m layer stated above and Eq. (3), a λ_{crit} of 1.6 km results. Wavelengths less than this value are unstable. The coherent wave detected in the middle of the isobaric leg has a wavelength of 3 km, which is twice as large as λ_{crit} and thus can persist for some time so that it is readily observable. For reference, if a 100-m layer had wind shear of $10\,\mathrm{m\,s^{-1}}$ and a change of virtual potential temperature of 3 K in a layer average temperature of 287 K, then λ_{crit} is 3 km. The ratio of λ_{crit} to the depth of the layer ($\lambda_{\mathrm{crit}}/\Delta z$) is ~7.5 (Miles and Howard 1964). A perturbation wave that develops near a λ_{crit} of 1.6 km has a breaking wave depth of 210 m, which is about the same size as the depth of the middle layer in Fig. 10a.

Evidence from the lidar and a wide range of in situ measurements supports the idea that turbulence generated though KHI is occurring just above the MBL. A different flight strategy targeted at measuring these processes would have to have been employed to provide more definitive measurements. The flight on 24 May 2012 was not specifically designed to observe this sort of processes, and it was an unexpected, but serendipitous, set of observations that point to the existence and major influence of KHI above the supercritical MBL that is responsible for a three-layer structure.

e. Summary of proposed conceptual model

Development of the middle well-mixed layer above the MBL is thought to take place over three main stages as illustrated in a conceptual model of an alongshore cross section and sounding (Fig. 13). Initially, a well-mixed MBL is capped by an inversion layer and the free troposphere above. This cross section represents the response of a supercritical flow near an inland bend of the coastline such as that south of Point Buchon. In this case, the depth of the MBL would thin downwind of the point and into the bay, and the winds would undergo a corresponding acceleration. The maximum alongshore wind speed is located near the top of the inversion layer.

The initial state does not necessarily have to be associated with a small Ri_b. To make it to the second stage, the Ri_b must decrease. As the wind accelerates into the expansion fan, vertical wind shear will increase. KHI is possible if the increase of wind shear is sufficient to overcome the thermal stability (i.e., low Ri_b). There is typically a pronounced diurnal cycle of coastal MBL depth and wind speed at the top of the MBL (e.g., Burk and Thompson 1996) that modulates the wind shear and thus the Ri_b. As a result, the morning to afternoon transition is the most likely time to progress from the initial state to the second state.

After the Ri_b decreases sufficiently and a perturbation develops that is smaller than a λ_{crit}, these perturbations will grow and eventually overturn. A greatly exaggerated overturning is used in the cross section at time t_1 to represent the overturning. Note that the scale is much smaller than the structures seen on the upwind (left) side the isobaric lidar image (Fig. 11). In fact, large wavelengths are stable while small wavelengths are not. The initial overturning will break into turbulent flow cascading down through a range of smaller scales, often transitioning from a cat's eye structure to stretched filaments. The middle portion of the initial overturning will become well mixed by the initial turbulence generated in this layer, which will dissipate downstream and is consistent with the observed decrease of EDR.

Downstream of the initial overturning is a redistribution of momentum and stability such that a middle layer of nearly neutral stability develops that is bounded above and below by narrow layers of stability. The redistribution of stability has also been inferred from radar for upper-troposphere occurrences of Kelvin–Helmholtz billows associated with clear air turbulence (e.g., Browning and Watkins 1970). Features in sounding 19 (Fig. 10) are consistent with the final stage of the conceptual model. The depth of the middle layer is also on the order of what would be predicted from the idealized theory.

Development of the middle layer can also be depicted in a more Lagrangian sense. Profiles in Fig. 14 show an alongshore progression of the temperature and wind profiles. Sounding selection is not exactly sampled along a trajectory so results are somewhat confounded by a flight pattern that was not designed to measure this unexpected phenomenon; soundings along the alongshore isobaric leg would have been ideal. Nevertheless, the key features are present. From the northernmost sounding 31 to sounding 22, the wind shear within the inversion layer increases and the stability of the inversion layer weakens. Finally, the vertical structure in sounding 19 depicts the clear development of a middle layer.

4. Conclusions

Essential characteristics of the low-level flow near the west coast of the United States during the warm season

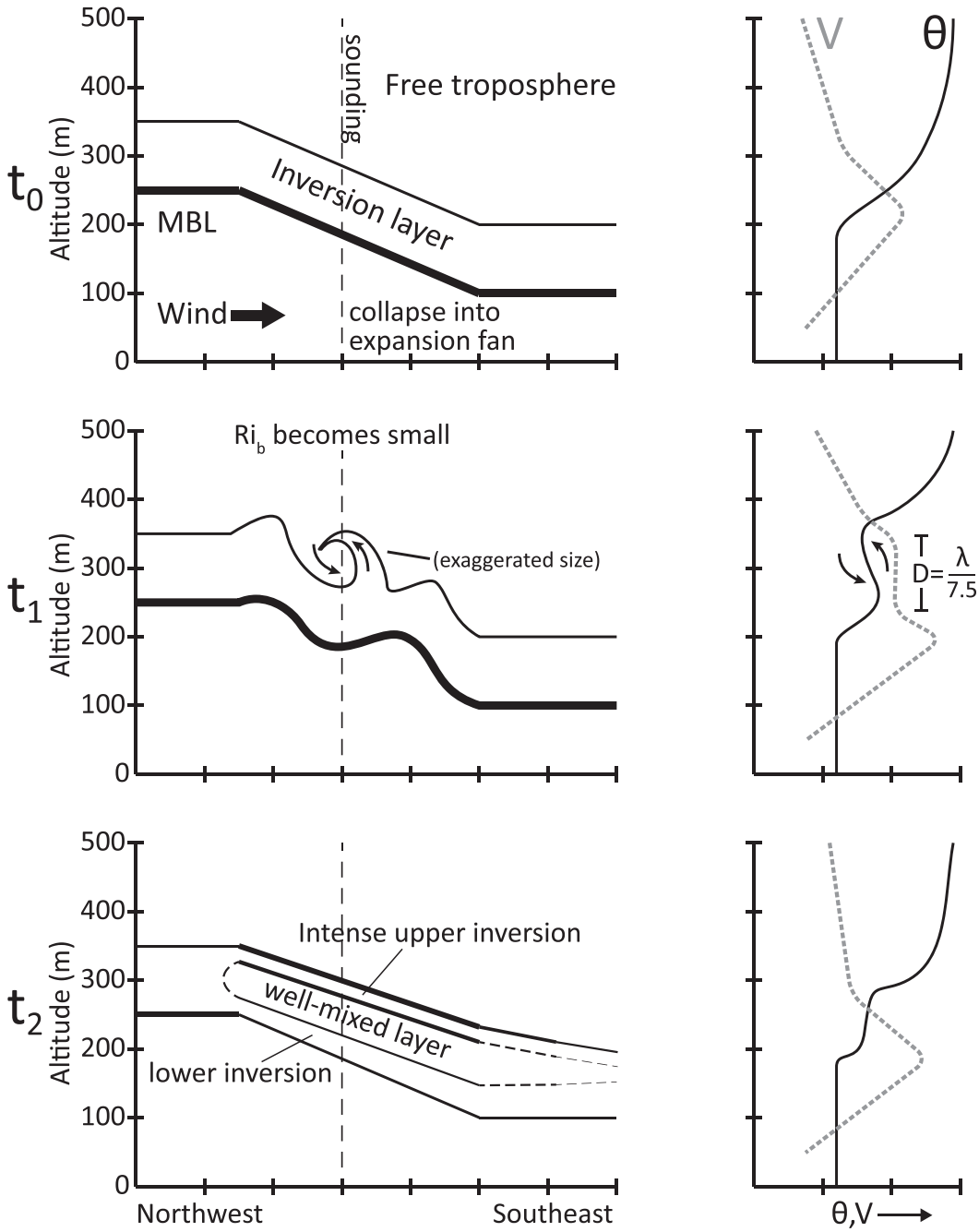

FIG. 13. Proposed conceptual model of the formation of the middle well-mixed layer seen in Figs. 8–10. (left) Alongshore cross section depicting the layers and (right) sounding corresponding to the vertical dashed line showing the alongshore wind speed V and potential temperature θ. Scale of turbulent overturning is greatly exaggerated in the t_1 cross section.

are typically represented as a two-layer (MBL and free troposphere) system that is bounded laterally by the coastal topography that rises above the depth of the MBL. If the Froude number is supercritical or transcritical, hydraulic features such as compression bulges and expansion fans manifest as local extrema in wind speed near points and capes along the coast. Aircraft observations taken during PreAMBLE on the particularly windy day of 24 May 2012 were designed to capture these hydraulic features between the Santa Barbara Channel and Monterey Bay. Near Point Buchon, a peculiar, secondary well-mixed layer above the main MBL

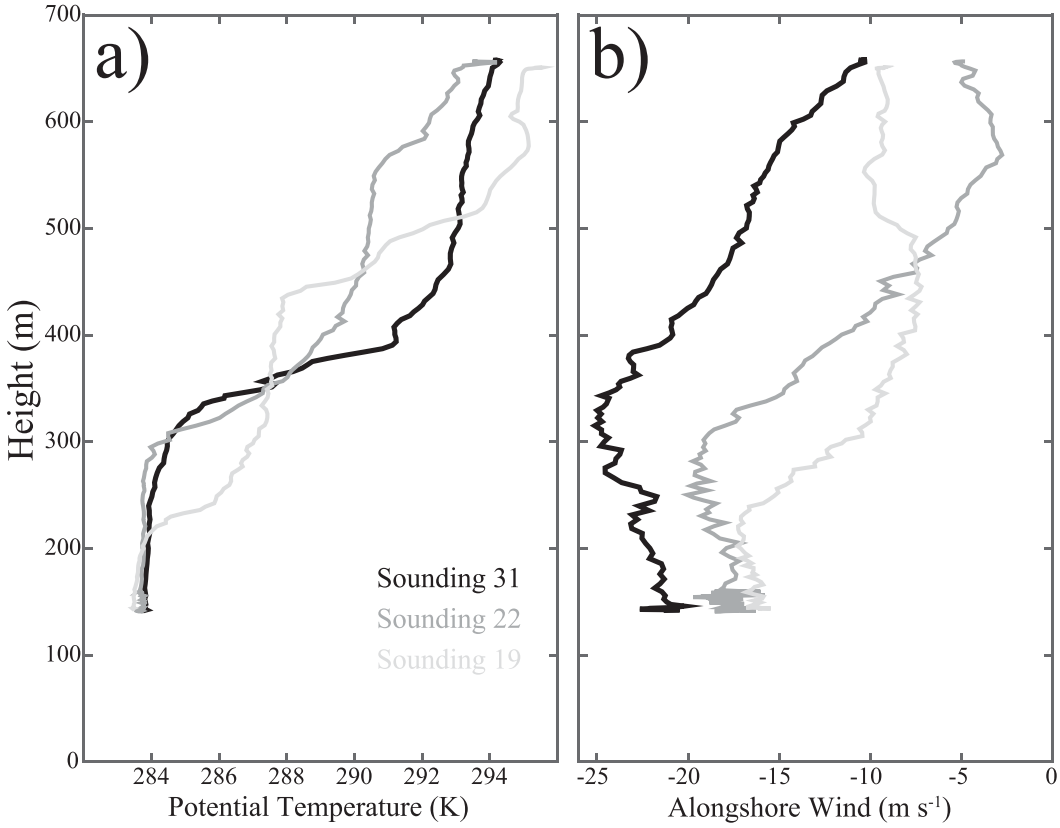

FIG. 14. (a) Potential temperature (K) and (b) alongshore wind component ($m\,s^{-1}$) for soundings 31 (black), 22 (gray), and 19 (light gray).

was observed above an expansion fan. The deviation from just a MBL that was capped by the free troposphere above has several important implications. These include impacts on the entrainment at the top of the MBL and modifications to the refractivity structure of the lower atmosphere that influences the propagation of electromagnetic radiation with consequences for radar detection and communication systems, which have been cited as a concern for national security (e.g., Burk and Thompson 1997; Brooks et al. 1999; Haack and Burk 2001; C. Wang et al. 2012).

Since the secondary well-mixed layer above the MBL was such a distinct and unexpected feature, an explanation of how it could have formed was sought. The existence of such a structure is not entirely unheard of. A similar structure has been observed with radiosondes in a low-level coastal jet in the afternoon along the shore of central Chile (Rahn et al. 2011). For that case, there was a local maximum of offshore flow within the middle layer that was thought to contribute to its formation. For the 24 May 2012 case in California, however, the offshore wind is not a factor and cannot be used to explain the existence of the secondary well-mixed layer.

Measurements presented here exhibit a large amount of alongshore wind shear, which pointed to KHI as the mechanism responsible for generating the secondary well-mixed layer. To explore this possibility, the Ri_b was calculated from several soundings along the coast. A small Ri_b suggests the development of KHI, which can greatly modify the nearshore environment. The Ri_b within the inversion layer at the top of the MBL decreases toward Point Buchon. Above the MBL in the vicinity of an expansion fan by Point Buchon, in situ and lidar observations reveal a secondary well-mixed layer bounded by two narrow layers of high stability: one of the high stability layers separates the secondary layer from the MBL below and the other high stability layer separates the secondary layer from the free troposphere above. Development of the secondary layer downwind of the low Ri_b is consistent with the expected behavior of KHI, including an observed depth on the same order as the depth calculated from idealized formulations of KHI. The environment is drastically altered from a two-layer to a three-layer structure, at least in the vicinity of the expansion fan. Offshore, subsiding flow aloft only appears to enhance the uppermost inversion layer

between the middle layer and the free troposphere above, but it does not appear to play any role in forming the middle layer.

Although these processes can be viewed as secondary to the fundamental two-layer shallow-water model that explains the major features such as the presence of an expansion fan, they do have a significant impact on the lower atmosphere. Near coastal features such as Point Buchon, conditions are often favorable for large wind shear given the relatively strong and persistent coastal low-level jet during the warm season. Furthermore, there is a natural variation of wind shear occurring diurnally. Point Buchon is an ideal location for more targeted boundary layer studies under a range of Ri_b.

Acknowledgments. This research was supported in part by the National Science Foundation through Grants AGS-1439515 and AGS-1439594. The field project was supported by AGS-1034862. The authors wish to thank pilots Ahmad Bandini and Brett Wadsworth and scientists Jeff French and Larry Oolman for help with the PreAMBLE field study and UWKA measurements. The comments and suggestions of three anonymous reviewers are gratefully acknowledged.

REFERENCES

Brooks, I. M., A. K. Goroch, and D. P. Rogers, 1999: Observations of strong surface radar ducts over the Persian Gulf. *J. Appl. Meteor.*, **38**, 1293–1310, doi:10.1175/1520-0450(1999)038<1293:OOSSRD>2.0.CO;2.

Browning, K. A., and C. D. Watkins, 1970: Observations of clear air turbulence by high power radar. *Nature*, **227**, 260–263, doi:10.1038/227260a0.

Burk, S. D., and W. T. Thompson, 1996: The summertime low-level jet and marine boundary layer structure along the California coast. *Mon. Wea. Rev.*, **124**, 668–686, doi:10.1175/1520-0493(1996)124<0668:TSLLJA>2.0.CO;2.

——, and ——, 1997: Mesoscale modeling of summertime refractive conditions in the Southern California bight. *J. Appl. Meteor.*, **36**, 22–31, doi:10.1175/1520-0450(1997)036<0022:MMOSRC>2.0.CO;2.

——, T. Haack, and R. M. Samelson, 1999: Mesoscale simulation of supercritical, subcritical, and transcritical flow along coastal topography. *J. Atmos. Sci.*, **56**, 2780–2795, doi:10.1175/1520-0469(1999)056<2780:MSOSSA>2.0.CO;2.

Cushman-Roisin, B., 2005: Kelvin–Helmholtz instability as a boundary-value problem. *Environ. Fluid Mech.*, **5**, 507–525, doi:10.1007/s10652-005-2234-0.

Dorman, C. E., and D. Koračin, 2008: Response of the summer marine layer flow to an extreme California coastal bend. *Mon. Wea. Rev.*, **136**, 2894–2992, doi:10.1175/2007MWR2336.1.

——, D. P. Rogers, W. Nuss, and W. T. Thompson, 1999: Adjustment of the summer marine boundary layer around Point Sur, California. *Mon. Wea. Rev.*, **127**, 2143–2159, doi:10.1175/1520-0493(1999)127<2143:AOTSMB>2.0.CO;2.

Ďurán, I. B., J.-F. Geleyn, and F. Váňa, 2014: A compact model for the stability dependency of TKE production–destruction–conversion terms valid for the whole range of Richardson numbers. *J. Atmos. Sci.*, **71**, 3004–3026, doi:10.1175/JAS-D-13-0203.1.

Edwards, K. A., A. M. Rogerson, C. D. Winant, and D. P. Rogers, 2001: Adjustment of the marine atmospheric boundary layer to a coastal cape. *J. Atmos. Sci.*, **58**, 1511–1528, doi:10.1175/1520-0469(2001)058<1511:AOTMAB>2.0.CO;2.

Feng, X., 2001: Evaluation of the MacCready turbulence sensor. M.S. thesis, Dept. of Atmospheric Science, University of Wyoming, 81 pp.

Gaiser, P. W., and Coauthors, 2004: The WindSat spaceborne polarimetric microwave radiometer: Sensor description and early orbit performance. *IEEE Trans. Geosci. Remote Sens.*, **42**, 2347–2361, doi:10.1109/TGRS.2004.836867.

Grisogono, B., and D. Belušić, 2008: Improving mixing length-scale for stable boundary layers. *Quart. J. Roy. Meteor. Soc.*, **134**, 2185–2192, doi:10.1002/qj.347.

Haack, T., and S. D. Burk, 2001: Summertime marine refractivity conditions along coastal California. *J. Appl. Meteor.*, **40**, 673–687, doi:10.1175/1520-0450(2001)040<0673:SMRCAC>2.0.CO;2.

——, ——, C. Dorman, and D. Rodgers, 2001: Supercritical flow interaction within the Cape Blanco–Cape Mendocino orographic complex. *Mon. Wea. Rev.*, **129**, 688–708, doi:10.1175/1520-0493(2001)129<0688:SFIWTC>2.0.CO;2.

Howard, L. N., 1961: Note on a paper of John Miles. *J. Fluid Mech.*, **10**, 509–512, doi:10.1017/S0022112061000317.

MacCready, P. B., Jr., 1964: Standardization of gustiness values from aircraft. *J. Appl. Meteor.*, **3**, 439–449, doi:10.1175/1520-0450(1964)003<0439:SOGVFA>2.0.CO;2.

Miles, J. W., 1961: On the stability of heterogeneous shear flows. *J. Fluid Mech.*, **10**, 496–508, doi:10.1017/S0022112061000305.

——, and L. N. Howard, 1964: Note on a heterogeneous shear flow. *J. Fluid Mech.*, **20**, 331–336, doi:10.1017/S0022112064001252.

Parish, T. R., and D. Leon, 2013: Measurement of cloud perturbation pressures using an instrumented aircraft. *J. Atmos. Oceanic Technol.*, **30**, 215–229, doi:10.1175/JTECH-D-12-00011.1.

——, M. D. Burkhart, and A. R. Rodi, 2007: Determination of the horizontal pressure gradient force using global positioning system onboard an instrumented aircraft. *J. Atmos. Oceanic Technol.*, **24**, 521–528, doi:10.1175/JTECH1986.1.

——, D. A. Rahn, and D. Leon, 2014: Aircraft observations of the marine boundary layer adjustment near Point Arguello, CA. *J. Appl. Meteor. Climatol.*, **53**, 970–989, doi:10.1175/JAMC-D-13-0164.1.

Rahn, D. A., R. D. Garreaud, and J. A. Rutllant, 2011: The low-level atmospheric circulation near Tongoy Bay–point Lengua de Vaca (Chilean coast, 30°S). *Mon. Wea. Rev.*, **139**, 3628–3647, doi:10.1175/MWR-D-11-00059.1.

——, T. R. Parish, and D. Leon, 2013: Airborne measurements of coastal jet transition around Point Conception, California. *Mon. Wea. Rev.*, **141**, 3827–3839, doi:10.1175/MWR-D-13-00030.1.

——, ——, and ——, 2014: Coastal jet adjustment near Point Conception, California, with opposing wind in the bight. *Mon. Wea. Rev.*, **142**, 1344–1360, doi:10.1175/MWR-D-13-00177.1.

Rodi, A. R., and P. A. Spyers-Duran, 1972: Analysis of time response of airborne temperature sensors. *J. Appl. Meteor.*, **11**, 554–556, doi:10.1175/1520-0450(1972)011<0554:AOTROA>2.0.CO;2.

Rogers, D. P., and Coauthors, 1998: Highlights of coastal waves 1996. *Bull. Amer. Meteor. Soc.*, **79**, 1307–1326, doi:10.1175/1520-0477(1998)079<1307:HOCW>2.0.CO;2.

Rogerson, A. M., 1999: Transcritical flows in the coastal marine atmospheric boundary layer. *J. Atmos. Sci.*, **56**, 2761–2779, doi:10.1175/1520-0469(1999)056<2761:TFITCM>2.0.CO;2.

Saha, S., and Coauthors, 2010: The NCEP Climate Forecast System Reanalysis. *Bull. Amer. Meteor. Soc.*, **91**, 1015–1057, doi:10.1175/2010BAMS3001.1.

Samelson, R. M., 1992: Supercritical marine-layer flow along a smoothly varying coastline. *J. Atmos. Sci.*, **49**, 1571–1584, doi:10.1175/1520-0469(1992)049<1571:SMLFAA>2.0.CO;2.

——, and S. J. Lentz, 1994: The horizontal momentum balance in the marine atmospheric boundary layer during CODE-2. *J. Atmos. Sci.*, **51**, 3745–3757, doi:10.1175/1520-0469(1994)051<3745:THMBIT>2.0.CO;2.

Scorer, R. S., 1969: Mechanism of clear air turbulence. *Clear Air Turbulence and Its Detection*, Y.-H. Pao and A. Goldburg, Eds., Plenum Press, 34–50.

Sharman, R. D., L. B. Cornman, G. Meymaris, J. Pearson, and T. Farrar, 2014: Description and derived climatologies of automated in situ eddy-dissipation-rate reports of atmospheric turbulence. *J. Appl. Meteor. Climatol.*, **53**, 1416–1432, doi:10.1175/JAMC-D-13-0329.1.

Smyth, W. D., and W. R. Peltier, 1989: The transition between Kelvin–Helmholtz and Holmboe instability: An investigation of the overreflection hypothesis. *J. Atmos. Sci.*, **46**, 3698–3720, doi:10.1175/1520-0469(1989)046<3698:TTBKAH>2.0.CO;2.

Strauss, L., S. Serafin, S. Haimov, and V. Grubišić, 2015: Turbulence in breaking mountain waves and atmospheric rotors estimated from airborne in situ and Doppler radar measurements. *Quart. J. Roy. Meteor. Soc.*, **141**, 3207–3225, doi:10.1002/qj.2604.

Stull, R. B., 1988: *An Introduction to Boundary Layer Meteorology*. Kluwer Academic, 666 pp.

Tjernström, M., and B. Grisogono, 2000: Simulations of supercritical flow around points and capes in a coastal atmosphere. *J. Atmos. Sci.*, **57**, 108–135, doi:10.1175/1520-0469(2000)057<0108:SOSFAP>2.0.CO;2.

Troy, C. D., and J. R. Koseff, 2005: The instability and breaking of long internal waves. *J. Fluid Mech.*, **543**, 107–136, doi:10.1017/S0022112005006798.

Veneziani, M., C. A. Edwards, and A. M. Moore, 2009: A central California coastal ocean modeling study: 2. Adjoint sensitivities to local and remote forcing mechanisms. *J. Geophys. Res.*, **114**, C04020, doi:10.1029/2008JC004775.

Wang, C., D. Wilson, T. Haack, P. Clark, H. Lean, and R. Marshall, 2012: Effects of initial and boundary conditions of mesoscale models on simulated atmospheric refractivity. *J. Appl. Meteor. Climatol.*, **51**, 115–132, doi:10.1175/JAMC-D-11-012.1.

Wang, Z., P. Wechsler, W. Kuestner, J. French, A. Rodi, B. Glover, M. Burkhart, and D. Lukens, 2009: Wyoming Cloud Lidar: Instrument description and applications. *Opt. Express*, **17**, 13 576–13 587, doi:10.1364/OE.17.013576.

——, and Coauthors, 2012: Single aircraft integration of remote sensing and in situ sampling for the study of cloud microphysics and dynamics. *Bull. Amer. Meteor. Soc.*, **93**, 653–668, doi:10.1175/BAMS-D-11-00044.1.

Winant, C. D., C. E. Dorman, C. A. Friehe, and R. C. Beardsley, 1988: The marine boundary layer off Northern California: An example of supercritical channel flow. *J. Atmos. Sci.*, **45**, 3588–3605, doi:10.1175/1520-0469(1988)045<3588:TMLONC>2.0.CO;2.

Yih, C.-S., 1969: A class of solutions for steady stratified flows. *J. Fluid Mech.*, **36**, 75–85, doi:10.1017/S0022112069001522.

Zilitinkevich, S., T. Elperin, N. Kleeorin, and I. Rogachevskii, 2007: Energy-and flux-budget (EFB) turbulence closure model for stably stratified flows. Part I: Steady-state, homogeneous regimes. *Bound.-Layer Meteor.*, **125**, 167–192, doi:10.1007/s10546-007-9189-2.